remote sensing

MDPI

Article

Dominant Factor in the Relationship Between Ice Thickness and Flow Velocity in the Downstream Region of Shirase Glacier, East Antarctica, Derived from Remotely Sensed Data

Kazuki Nakamura [1,*], Yurina Satake [2], Tsutomu Yamanokuchi [3] and Shigeru Aoki [4]

[1] College of Engineering, Nihon University, 1 Nakagawara, Tokusada, Tamura-machi, Koriyama, Fukushima 963-8642, Japan
[2] Graduate School of Engineering, Nihon University, 1 Nakagawara, Tokusada, Tamura-machi, Koriyama, Fukushima 963-8642, Japan; ceyu24001@g.nihon-u.ac.jp
[3] Remote Sensing Technology Center of Japan, TOKYU REIT Toranomon Bldg.2F 3-17-1 Toranomon, Mina-to-ku, Tokyo 105-0001, Japan; tsutomuy@restec.jp
[4] Institute of Low Temperature Science, Hokkaido University, Kita-19, Nishi-8, Kita-ku, Sapporo 060-0819, Japan; shigeru@lowtem.hokudai.ac.jp
* Correspondence: nakamura.kazuki@nihon-u.ac.jp

Highlights

What are the main findings?

- Decadal satellite observations (2016–2025) revealed that the Shirase Glacier's flow velocity accelerates immediately when surrounding landfast ice becomes unstable, while ice thickness potentially decreases with a time lag of zero to two years.
- Basal melt rates vary spatially, peaking at approximately 20 m a^{-1} near the grounding line due to modified Circumpolar Deep Water (mCDW) and increasing again near the ice front due to warm summer surface waters.

What are the implications of the main findings?

- The results quantitatively demonstrate the critical "buttressing effect" of landfast ice, showing that its loss triggers rapid dynamical responses in the glacier before manifesting as physical mass loss (thinning).
- The study elucidates the complex interaction between glacier dynamics, landfast ice stability, and subglacial ocean circulation, providing essential data for monitoring the long-term stability of the East Antarctic Ice Sheet.

Abstract

The buttressing effect of landfast sea ice is crucial for the stability of Antarctic outlet glaciers. This study investigated spatiotemporal variations in flow velocity and ice thickness at the Shirase Glacier, East Antarctica, from 2016 to 2025 using ALOS-2/PALSAR-2 and CryoSat-2/SIRAL data. Flow velocity increased, and ice thickness decreased downstream, exhibiting a significant negative correlation ($r = -0.66$, $p < 0.05$). Notably, during periods of unstable landfast ice (2017–2018 and 2023–2025), substantial ice flow acceleration occurred in the downstream ice tongue. Furthermore, basal melt rates calculated using the Eulerian flux divergence method revealed high melting (16–20 m a^{-1}) near the grounding line, decreasing to 2–4 m a^{-1} mid-stream, and increasing to 4–8 m a^{-1} near the ice front. This distribution is consistent with the subglacial oceanic vertical thermal structure. These results quantitatively demonstrate the significant control of both landfast ice stability and subglacial ocean circulation on the spatiotemporal dynamics of the Shirase Glacier.

Check for updates

Academic Editors: Shin Nagai, Tee-Ann Teo and Hideki Kobayashi

Received: 28 September 2026
Revised: 5 November 2026
Accepted: 5 November 2026
Published: 9 November 2026

Copyright: © 2026 by the authors. Licensee MDPI, Basel, Switzerland. This article is an open access article distributed under the terms and conditions of the Creative Commons Attribution (CC BY) license.

Keywords: basal melt; ice thickness; flow velocity; Shirase Glacier; East Antarctica; ALOS-2; CryoSat-2

1. Introduction

The mass loss of the Antarctic Ice Sheet is primarily driven by the accelerated discharge in outlet glaciers and the thinning of ice shelves and floating ice tongues [1,2]. These floating ice margins extending into the ocean cause back pressure upstream through frictional resistance generated against the surrounding land-fast sea ice and the bedrock at the side and bottom (pinning points). This physical restraining force, known as the buttressing effect, plays a crucial role in suppressing inland ice from flowing directly into the ocean [3,4]. Consequently, the processes of thinning and collapse of the ice tongue, resulting from interactions with the ocean, can directly promote the retreat of the grounding line (GL) and the outflow of ice into the ocean. Hence, it is essential to assess the stability of the entire ice sheet by monitoring the dynamics of ice shelves and ice tongues.

Satellite observations from previous studies have shown that the loss of the buttressing effect can result in abrupt changes in the ice sheet. Indeed, in regions where ice shelf collapse or rapid thinning has occurred, vertical tensile stress has increased in the underlying glaciers that have lost their support, resulting in a drastic acceleration of flow, reaching up to several times the previous rate, and a rapid thinning of ice thickness [5,6]. Thus, ice shelves are not merely extensions of the ice sheet; they function as a form of "safety band" that directly regulates the dynamics of the GL and are indispensable for preserving the long-term stability of the entire ice sheet [7]. In recent years, it has become evident that not only thick ice shelves but also landfast sea ice play a significant mechanical role in stabilizing the termini of outlet glaciers [8,9]. The destabilization and breakup of landfast ice can trigger an immediate dynamic response, leading to rapid glacier acceleration.

1.1. Study Area: Shirase Glacier

The importance of the dynamical buttress effect exerted by such ice shelves and ice tongues is no exception even in the East Antarctic Ice Sheet (EAIS), which has been previously thought to be balanced. Recent detailed observations have revealed ice mass loss in the region surrounding the Shirase Glacier (Figure 1), which accounts for one of the largest sources of ice outflow in East Antarctica [10]. The Shirase Glacier, one of the fastest-flowing outlet glaciers in East Antarctica, is a key region for understanding these complex ice–ocean interactions.

Previous in situ oceanographic and remote sensing studies have observed significant basal melting beneath the Shirase Glacier tongue, which is strongly linked to the intrusion of warm modified Circumpolar Deep Water (mCDW) into Lützow-Holm Bay [11,12]. The thinning of the ice tongue caused by this basal melting directly reduces the buttressing effect on the upstream region of the glacier. Furthermore, recent GNSS and satellite monitoring have demonstrated that the flow velocity of the Shirase Glacier is highly sensitive to the physical presence and stability of landfast ice in the bay, changing its velocity through the modulation of back pressure [13,14].

1.2. Research Objectives

Despite these critical findings, a comprehensive understanding of the spatiotemporal evolution of the Shirase Glacier remains elusive. Specifically, while the immediate velocity response to landfast ice collapse has been reported, the quantitative time-lagged physical response of the ice thickness, as well as the high-resolution spatial distribution of basal melt

rates along the floating tongue, have not been fully resolved using decadal-scale satellite observations. Addressing this research gap is essential for accurately quantifying the physical mass loss processes of the Shirase Glacier under changing ocean and sea-ice conditions.

In order to understand and continuously monitor long-term trends in the mass balance of the EAIS, it is necessary to measure the dynamics of not only flow velocities, but also ice thickness at the Shirase Glacier. Therefore, the objective of this study is to quantitatively assess the interannual variations in flow velocity and ice thickness at the Shirase Glacier tongue using continuous satellite observation data. In addition, through these integrated analyses, we aim to elucidate the physical processes that drive the spatiotemporal variations in the ice tongue.

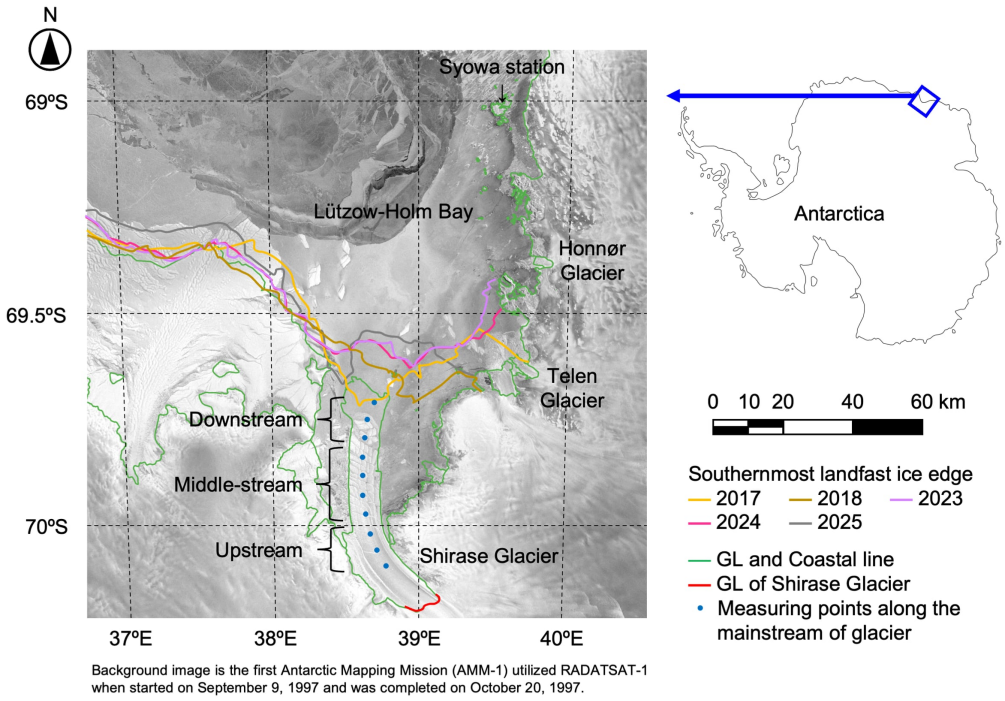


Figure 1. Map of the Shirase Glacier and Lützow-Holm Bay, East Antarctica. The inset map indicates the geographical location of the study area within Antarctica. The red line indicates the grounding line (GL) of the Shirase Glacier, while the green line shows the GL of other glaciers and the coastline [15]. Blue dots indicate the measuring points for ice thickness and flow velocity along the main stream of the glacier, which is divided into three subregions (upstream, middle-stream, and downstream) for subsequent analyses. The colored lines delineate the southernmost edges of the landfast sea ice during unstable conditions (2017, 2018, 2023, 2024, and 2025), derived from MODIS imagery [16]. The background is a RADARSAT-1 SAR image mosaic from the first Antarctic Mapping Mission (AMM-1), acquired between 9 September and 20 October 1997 [17].

2. Data and Methods

2.1. Flow Velocity Estimation

The Advanced Land Observing Satellite-2 (ALOS-2) was launched by the Japan Aerospace Exploration Agency (JAXA) on 24 May 2014, using the H-IIA Rocket No. 24. ALOS-2 has a 14-day revisit period and is equipped with the Phased Array type L-band Synthetic Aperture Radar-2 (PALSAR-2) instrument. Hence, PALSAR-2 can observe changes at the same location on the Shirase Glacier at intervals as short as 14 days. This study used HH-polarization data acquired in the Strip Map mode with the ascending orbit, which provides a nominal spatial resolution of approximately 10 m. A total of 87 image pairs were available to analyze changes in the Shirase Glacier during the period from April 2016 to

July 2025. Specifically, seven image pairs were acquired with an incident angle of 32° at the scene center of path number 193 from April 2016 to October 2018, and 80 image pairs were acquired with an incident angle of 42° at the scene center of path number 195 from July 2018 to July 2025. Table 1 lists the number of PALSAR-2 image pairs, and Tables A1 and A2 summarize their details.

Table 1. The number of PALSAR-2 images.

Year	Image Pair
2016	2
2017	3
2018	6
2019	20
2020	14
2021	10
2022	9
2023	10
2024	7
2025	6

Since the data was Single Look Complex (SLC) for image pairs in the radar coordinate system (range-azimuth coordinate system), we obtained amplitude images after performing co-registration, projected them into the map coordinate system, and estimated the flow velocity by calculating the flow offset using the offset tracking method. The offset tracking method involves detecting the same location within an image pair by comparing the alignment of small regions extracted from both images. Specifically, the spatial cross-correlation was calculated using a correlation window size of 128 × 128 pixels, which corresponds to approximately 1.05 km^2 (1.02 × 1.02 km). This size setting was optimized to effectively match the scale of iceberg fragments and persistent surface features such as crevasses. To ensure data quality, we applied the rejection criteria; tracking results with low correlation (<0.10) were filtered out as outliers. Furthermore, to generate the annual flow velocity fields, the horizontal displacement fields derived from individual image pairs within each year (Tables A1 and A2) were temporally composed by stacking and averaging the valid pixels. The offset tracking method is described in [13], along with an estimation of the error in the flow velocity derived by this method. To evaluate the accuracy of our flow velocity estimates, we compared the PALSAR-2 offset tracking results directly with continuous in situ GNSS measurements previously installed on the Shirase Glacier [13]. This direct validation yielded a root mean square error (RMSE) of 0.049 km a^{-1} (49 m a^{-1}). Given that the downstream flow velocity of the Shirase Glacier exceeds 2.0 km a^{-1}, this error margin represents less than 2% of the absolute velocity. This magnitude of uncertainty is highly consistent with, and generally comparable to, the accepted error margins (typically tens of meters per year) reported in other satellite-based offset tracking studies over fast-flowing Antarctic outlet glaciers [18]. Therefore, this confirms that our velocity dataset maintains sufficient reliability for analyzing interannual variability.

It should be noted that the ALOS-2 data acquisitions were switched from path 193 (incidence angle 32°) to path 195 (incidence angle 42°) in July 2018 due to an update in the Basic Observation Scenario operated by JAXA. While this switch altered the radar incidence angle, our offset tracking method derives horizontal displacements by maximizing the spatial cross-correlation of amplitude image patches (i.e., pixel matching of persistent surface features such as crevasses), rather than relying on interferometric phase differences. Consequently, the change in incidence angle has a negligible effect on the horizontal velocity estimations. The temporal consistency of the derived flow velocity across this

path switch is also empirically supported by the highly accurate GNSS validation results (RMSE = 0.049 km a^{-1}) mentioned above.

2.2. Ice Thickness Estimation

The CryoSat-2 satellite was launched by the European Space Agency (ESA) aboard a Dnepr-1 rocket on 8 April 2010. It has an orbital period of 369 days and a sub-cycle of 30 days and is equipped with a Synthetic Aperture Interferometric Radar Altimeter (SIRAL). This study uses the SIRAL data acquired in the Synthetic Aperture Interferometric (SIN) mode from January 2016 to December 2025, providing an along-track spatial resolution of approximately 250 m. This is because the Shirase Glacier is located on the coastal edge of the ice sheet, which is connected to the southern part of Lützow-Holm Bay (hereinafter referred to as LHB), and is observed in SIN mode. Table 2 lists the number of tracks used for the SIRAL data and the number of data points before and after quality control, and Table A3 summarizes the details of the SIRAL data acquisition dates. The Shirase Glacier tongue is heavily crevassed and features steep surface slopes, which frequently cause severe waveform snagging in the SIRAL radar altimeter. During the quality control (QC) process, to ensure elevation reliability, we strictly removed data points with low backscatter power or distorted waveforms. Consequently, the data volume was significantly reduced (68–81%). However, this rigorous screening is essential to eliminate erroneous measurements, ensuring that the remaining data maintain high accuracy. Despite this sparse sampling, the overall spatiotemporal trends remain robust and are sufficient for our decadal analysis.

Table 2. The number of SIRAL data used in this study and the removed ratio after quality control.

Year	Observation Tracks	Measuring Points		Removed Ratio
		Original	After Quality Control	
2016	14	974	253	74.0%
2017	10	846	159	81.2%
2018	10	1008	272	73.0%
2019	10	994	267	73.1%
2020	9	991	202	79.6%
2021	11	1065	302	71.6%
2022	11	1211	388	68.0%
2023	10	934	297	68.2%
2024	14	981	382	61.1%
2025	13	811	203	75.0%

The SIRAL can measure ellipsoidal heights based on the WGS-84 reference ellipsoid, and hence the freeboard was calculated using the geoid height from EGM2008 [19]. Since the ice tongue of the Shirase Glacier floats in the ocean, hydrostatic equilibrium was assumed to convert the freeboard to ice thickness. Note that the region analyzed in this study starts from 15 km downstream of the grounding line. Because the hinge zone, where grounding-zone dynamics such as tidal flexure and bridging stresses are significant, is typically limited to within several km of the grounding line (e.g., [20]), our 15 km starting point ensures that the glacier tongue is fully floating. Thus, the hydrostatic equilibrium assumption is strictly valid, and the direct influence of grounding-line dynamics on our thickness estimates is considered negligible. A comprehensive overview of ice thickness estimation based on the assumption of hydrostatic equilibrium is provided in [21]. However, they did not consider the effect of snow cover, such as the subsidence of the ice mass due to the load from snow and the propagation delay of the SIRAL microwaves as they travel through the snow. Therefore, this study recalculated the ice thickness by incorporating the snow on the ice into the procedure described by [21].

Assuming hydrostatic equilibrium, the ice floating in seawater experiences a buoyant force equal to the weight of the seawater displaced by the ice, and hence, Equation (1) holds.

$$\rho_{ice} \times S \times h_{ice} \times g + \rho_{snow} \times S \times h_{snow} \times g = \rho_{sea} \times S \times (h_{ice} - f) \times g, \quad (1)$$

Here, ρ_{snow}, ρ_{ice} and ρ_{sea} are the densities of snow, ice, and seawater, respectively; S is the base area of the ice; h_{snow} is the snow depth; h_{ice} is the ice thickness; g is the gravitational acceleration; and f is the freeboard. According to [21], ρ_{ice} and ρ_{sea} were set to 900 kg m^{-3} and 1030 kg m^{-3}, respectively, and ρ_{snow} was set to 300 kg m^{-3} based on the results of field surveys conducted around the Syowa Station [22]. The maximum snow depth for each year from the AMSR Research Product [23] was used as the representative value for h_{snow} in this study. The annual maximum snow depth was used instead of the annual mean because using the mean would likely underestimate the snow accumulation on the glacier. Such an underestimation would fail to adequately account for the mass contribution of the snow layer to the total freeboard in the hydrostatic equilibrium calculation. Therefore, the maximum value was selected to ensure that the snow loading effect is properly incorporated into the ice thickness retrieval. Table 3 summarizes the representative values of h_{snow} derived from this product.

Table 3. Annual statistics of snow depth over the Shirase Glacier tongue derived from the daily AMSR2 Level 3.0 Research Product. The annual maximum values were used for the hydrostatic equilibrium calculation.

Year	Maximum (m)	Mean (m)	SD (m)
2016	0.191	0.035	0.052
2017	0.220	0.056	0.070
2018	0.180	0.037	0.050
2019	0.180	0.033	0.054
2020	0.185	0.032	0.058
2021	0.180	0.020	0.045
2022	0.331	0.048	0.086
2023	0.231	0.029	0.059
2024	0.236	0.042	0.067
2025	0.241	0.040	0.075

Next, we considered the delay in the speed of microwave propagation of the SIRAL caused by snow cover δ_c [24], which can be expressed in the following formula of

$$\delta_c = h_{snow}\left(1 - \frac{C_s}{C}\right) \approx 0.22\, h_{snow}, \quad (2)$$

where C_s is the propagation speed of Ku-band microwaves penetrating snow, and C is the light speed in a vacuum.

By simplifying Equation (1) and incorporating δ_c in Equation (2), we obtain the following equation for calculating h_{ice} based on the magnitude of h_{snow}. The threshold of 0.20 m for the snow depth in Equation (3) is defined based on the penetration characteristics of the Ku-band radar and the uncertainty limits of the AMSR snow depth product. Over compacted firm and thin snow layers on the ice tongue, when the snow depth is extremely thin (<0.20 m), the main radar scattering horizon approaches the air–snow interface (e.g., [25]), and the estimated snow depth falls within the inherent margin of error of the AMSR product (0.173 m) [26]. Therefore, a simplified treatment of the snow layer is justified below this threshold to avoid overcorrecting the hydrostatic equilibrium calculation.

$$h_{ice} = \begin{cases} 7.92\, f + 4.05\, h_{snow} & (h_{snow} \geq 0.20) \\ 7.92\, f + 2.31\, h_{snow} & (h_{snow} < 0.20) \end{cases} \quad (3)$$

The error in the estimated ice thickness, δh_{ice}, is based on the error propagation of δf and δh_{snow}. δh_{ice}, and is calculated as

$$\delta h_{ice} = \sqrt{\left(\frac{\partial h_{ice}}{\partial f}\right)^2 \delta f^2 + \left(\frac{\partial h_{ice}}{\partial h_{snow}}\right)^2 \delta {h_{snow}}^2} \quad (4)$$

Here, δf is expressed as follows:

$$\delta f = \sqrt{\delta {h_e}^2 + \delta {h_g}^2}, \quad (5)$$

where δh_e is the error used to determine the ellipsoidal height of SIRAL, and δh_g is the geoid error. δh_e is attributed to speckle noise in the SARIn mode of SIRAL, which is caused by system errors [27]. The resultant δh_e was set to 0.14 m, and since the commission error of the EGM2008 was reported in [19], δh_g was set to 0.183 m. Therefore, δf was calculated to be 0.23 m. Additionally, δh_{snow} was set to 0.173 m, as JAXA published the mean absolute error of the snow depth product [26]. Finally, δh_{ice} was estimated to be $\pm$1.95 m when the snow depth is 0.20 m or greater, and $\pm$1.86 m when the snow depth is less than 0.20 m. Using these derived values, to generate the annual ice thickness profiles along the glacier centerline, the irregularly distributed CryoSat-2 measurement points within a $\pm$3 km width from the central streamline were extracted and spatially averaged at 5 km intervals, following the methodology established by Satake and Nakamura [21].

It should be noted that the error assessment presented above primarily considers measurement errors. Additional uncertainties may arise from the parameters and assumptions used in the hydrostatic equilibrium calculation. Specifically, ρ_{ice}, ρ_{snow} and ρ_{sea} were assumed to be constant, although they can vary spatiotemporally. A sensitivity analysis indicates that a 1% uncertainty in ice density (~9 kg m^{-3}) can introduce an absolute thickness error on the order of ~10 m. Furthermore, the sensitivity of the calculated ice thickness to snow depth is roughly a factor of four ($\partial h_{ice}/\partial h_{snow} \approx 4.05$). Furthermore, the assumption of perfect hydrostatic equilibrium may not fully account for internal bridging stresses within the heavily crevassed ice tongue. In addition, the estimation of snow depth introduces uncertainties related to the variable penetration depth of the Ku-band radar into the snowpack, which depends on the internal stratigraphy and snow density variations. However, because these systematic uncertainties act as a constant baseline offset over the decadal period, they largely cancel out when calculating relative interannual anomalies. Therefore, while absolute ice thickness values inherently contain greater systematic uncertainties, the relative interannual variations (which exhibit amplitudes of ~10 m) remain statistically robust and distinguishable from random measurement noise. Thus, these systematic biases are considered to have a minimal impact on the relative temporal correlations and the dynamic lag discussed in the following sections.

2.3. Basal Melt Rate Estimation

Assuming that the glacier is an incompressible fluid with a constant outflow width and density and that the direction of glacier flow is defined as the x-axis, with changes in that perpendicular direction being negligible, the flow can be expressed by Equation (6) based on the continuity equation [28].

$$\frac{\partial H}{\partial t} + \frac{\partial (uH)}{\partial x} = \dot{b}, \quad (6)$$

where H is ice thickness, u is flow velocity, t is time, and $\dot{b}$ is the mass balance (accumulation − ablation) at the surface and bottom of the glacier tongue.

We investigate the Eulerian flux divergence method based on the law of mass conservation (e.g., [2,29]) to estimate the basal melt rate of the Shirase Glacier using the

spatiotemporal variations in the flow velocity and ice thickness of the glacier obtained from satellite observations. Equation (7) can be obtained by rearranging Equation (6):

$$\dot{m} = \dot{a} - \frac{\partial H}{\partial t} - \left(u\frac{\partial H}{\partial x} + H\frac{\partial u}{\partial x} \right), \quad (7)$$

where $\dot{m}$ is the basal melt rate, and $\dot{a}$ is the surface accumulation rate derived from the monthly average surface mass balance (SMB) data from the regional atmospheric climate model (RACMO) version 2.4p1 [30]. Since the RACMO's SMB data are expressed in the water equivalent, they were converted to the ice equivalent using Equation (8):

$$SMB_{ice_eq} = \frac{SMB_{water_eq}}{1000} \times \frac{\rho_{smb_water}}{\rho_{smb_ice}}, \quad (8)$$

where SMB_{ice_eq} and SMB_{water_eq} are the ice equivalent (m a^{-1}) and water equivalent (mm w.e.), respectively, and ρ_{smb_water} and ρ_{smb_ice} are the densities of water (1000 kg m^{-3}) and ice (917 kg m^{-3}), respectively.

The RACMO's SMB data are grid-based and cover the area including the 15–25 km DGL of Shirase Glacier. These data were converted to SMB_{ice_eq} using Equation (9), the annual mean of which was calculated and used in this study. The annual accumulated SMB used ranged from 0.324 to 0.516 m a^{-1} during our analysis period (Table 4), which was very small compared to the other terms in Equation (7).

Table 4. Annual accumulated SMB used in this study.

Year	SMB (m a^{-1})
2016	0.516
2017	0.324
2018	0.468
2019	0.360
2020	0.324
2021	0.396
2022	0.432
2023	0.408
2024	0.516
2025	0.348

3. Results

3.1. Spatial Profiles of Flow Velocity and Ice Thickness

Figure 2 shows the estimated magnitudes of flow velocity and ice thickness along the central flow line of the Shirase Glacier (Figure 1). Previous studies have demonstrated that the Shirase Glacier's flow velocity is related to the stability or instability of the surrounding landfast ice in the LHB [31]. In this study, "unstable" is defined as the condition where the landfast ice physically breaks away and the collapse front reaches the immediate terminus (ice front) of the Shirase Glacier, directly removing the mechanical support. Conversely, "stable" is defined as the condition where the landfast ice remains intact and firmly connected to the glacier terminus, regardless of offshore breakouts further north. In 2015, no collapse or breakaway of the landfast ice reaching the glacier terminus was observed. Instead, offshore landfast ice broke away, with its southern boundary approximately 45 km north of the glacier terminus [32]. The following year, in 2016, the landfast ice at the glacier's ice front began to collapse and flow out. This trend continued through 2018 [31]. From 2019 onward, no collapse or breakaway of landfast ice reaching the glacier terminus was observed. However, in May 2023, the landfast ice breaking away and reaching the glacier terminus

was observed again. This situation continued into 2025. Hence, Figure 2 discriminates the flow velocity and ice thickness during periods of stable and unstable landfast ice conditions using open circles and crosses, respectively. The relationship between the condition of the landfast ice and the flow velocity and ice thickness is discussed later in subsections.

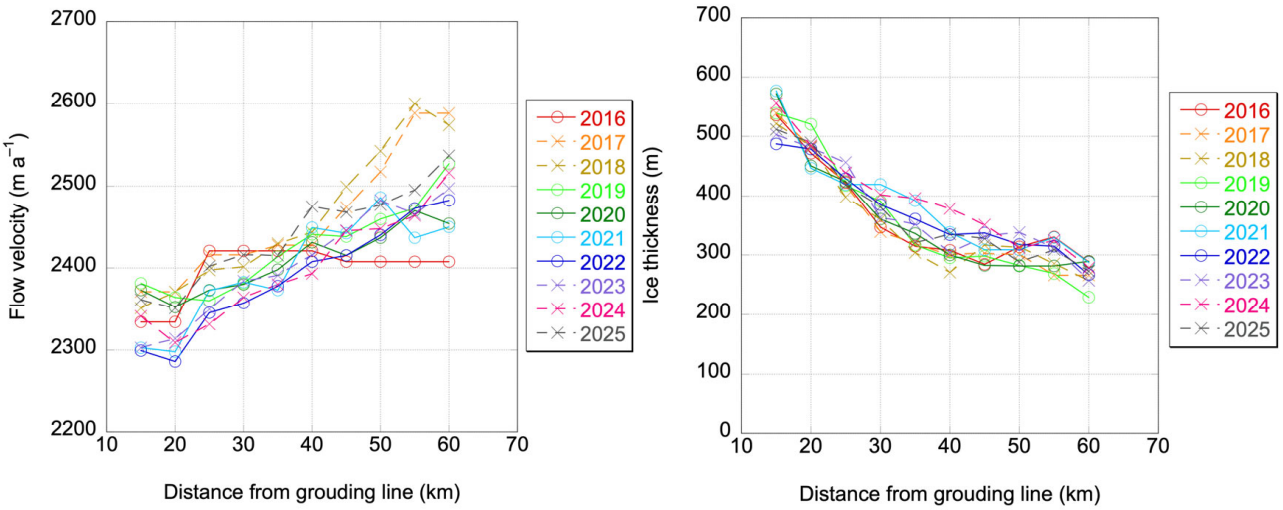


Figure 2. Profiles of (**a**) flow velocity and (**b**) ice thickness in the central streamline of the Shirase Glacier. Open circles and crosses indicate stable and unstable landfast ice conditions, respectively.

Figure 2a shows the results of applying the offset tracking method to ALOS-2/PALSAR-2 data to determine the flow velocity along the central streamline of the Shirase Glacier tongue. The horizontal axis of this figure is the distance from the GL toward the downstream (hereinafter referred to as downstream from GL: DGL), and the vertical axis is the annual mean flow velocity. The figure shows that the flow velocity of the Shirase Glacier tongue increased downstream from 15 to 60 km DGL throughout the 10-year period from 2016 to 2025. This spatial trend was consistent with the flow velocity distributions derived from JERS-1/SAR, ALOS/PALSAR, and ALOS-2/PALSAR-2 data [13,33], indicating the structure has continued for 30 years.

Figure 2b shows the ice thickness along the central streamline of the Shirase Glacier, derived from CryoSat-2/SIRAL data by applying the hydrostatic equilibrium assumption. The horizontal axis of this figure is the same as in Figure 2a, and the vertical axis is the annual mean ice thickness. The figure shows that the ice thickness of the glacier tongue decreased from 15 to 60 km DGL throughout the 2016–2025 period. This overall structure was consistent with the results obtained from the ALOS World 3D (AW3D30) [34] as a digital surface model (DSM) [21]. Furthermore, Figure 2 shows that the flow velocity had significant interannual variability in the downstream, while the ice thickness had greater variability in the middle of the stream of the glacier. To investigate the spatial characteristics of the interannual variability in flow velocity and ice thickness based on the decadal observation data, we calculated the standard deviations over the 10-year period for each DGL (Table 5). This revealed that the peaks of variation for flow velocity and ice thickness occurred in spatially distinct regions. Therefore, the ice tongue was divided into three subregions: upstream (15–25 km DGL), middle-stream (30–45 km DGL), and downstream (50–60 km DGL). The standard deviation of the interannual variation in flow velocity ranged from 21.4 to 31.4 m a^{-1} in the upstream and middle-stream regions, but it was found to increase significantly toward the downstream region, reaching a maximum of 60.9 m a^{-1} at 55 km DGL. This finding indicated that the interannual variation in flow

velocity responded with high sensitivity to changes in the dynamics of the landfast ice surrounding the glacier terminus. Conversely, the interannual variability in ice thickness showed a spatial distribution different from that of flow velocity, with the standard deviation peaking in the middle-stream region (32.5 m at 35 km DGL). The factors and processes driving these spatiotemporal variations in flow velocity and ice thickness are examined in detail in the following section.

Table 5. Annual mean ± SD of ice thickness and flow velocity at 15–60 km DGL.

Year	Ice Thickness (m)	Flow Velocity (m a^{-1})
2016	361.8 ± 85.4	2398.4 ± 34.5
2017	353.4 ± 93.8	2459.7 ± 80.3
2018	351.0 ± 89.6	2460.8 ± 87.7
2019	355.8 ± 106.8	2423.9 ± 54.0
2020	358.0 ± 96.8	2408.3 ± 39.2
2021	382.6 ± 87.6	2399.3 ± 64.2
2022	371.2 ± 72.8	2388.4 ± 67.8
2023	369.9 ± 81.8	2404.9 ± 68.7
2024	392.0 ± 83.5	2399.1 ± 66.8
2025	365.5 ± 82.4	2439.7 ± 60.2
Decadal mean ± SD	366.1 ± 88.1	2418.3 ± 62.3

3.2. Interannual Variability in Ice Thickness and Flow Velocity

Figure 3 shows the temporal variations in annual mean magnitudes of ice thickness and flow velocity over 15–60 km DGL of the Shirase Glacier tongue. The flow velocity generally increased in the years when the ice thickness decreased, and vice versa. A Pearson correlation analysis revealed a statistically significant negative correlation ($r = -0.66$, $p = 0.036$, $N = 10$, $df = 8$), which is less than the 5% significance level and thus indicates a statistically significant relationship. Hence, the negative correlation between ice thickness and flow velocity was shown not only for spatial variations but also for interannual variations.

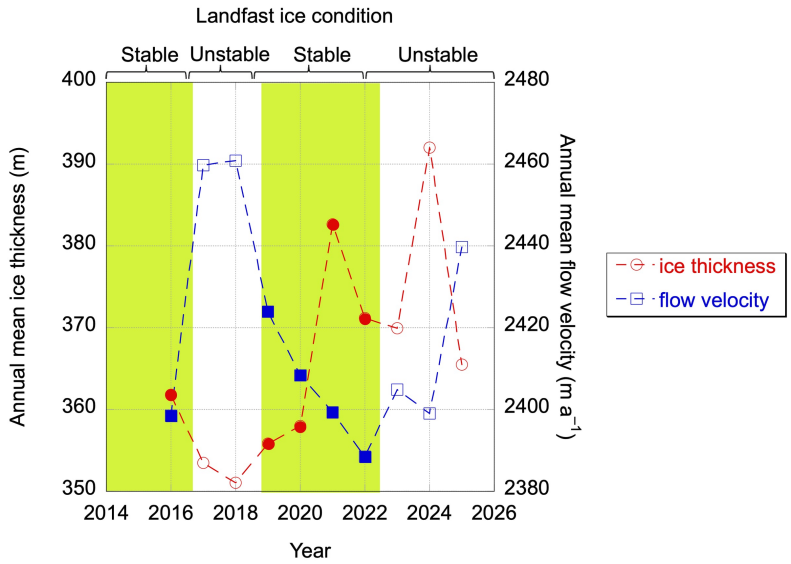


Figure 3. Fluctuations of annual mean ice thickness and flow velocity at 15–60 km DGL as the landfast ice conditions change. The solid and open plots indicate stable and unstable landfast ice, respectively. The yellow-green shaded areas indicate periods of stable landfast ice conditions in the LHB.

The annual variations were strongly associated with the stability of the landfast ice in the LHB. Table 5 summarizes the mean ice thickness and flow velocity at the 15–60 km

DGL of the glacier tongue. Although the mean ice thickness was 361.8 ± 1.95 m in 2016, it decreased by approximately 10 m from 2017 to 2018 due to the breakaway of the landfast ice. The mean flow velocity was 2398.4 ± 49.0 m a^{-1} in 2016; however, it increased by approximately 62 m a^{-1} from 2017 to 2018 due to the unstable condition of the landfast ice. Consequently, the highest value of 2460.8 ± 49.0 m a^{-1} was observed during the period in this study, and the thickness decreased to 351 ± 1.95 m. From 2019 to 2022, the landfast ice in the LHB was stable, and the flow velocity decreased to 2388.4 ± 49.0 m a^{-1}. In response to this recovery of the buttress effect, the ice thickness in the downstream region had also begun to increase gradually, although with a lag of one to two years. From 2023 onward, the flow velocity increased again by 51.3 m a^{-1} when the breakaway of landfast ice resumed. In response to this acceleration, the ice thickness decreased once again with a further time lag.

To investigate the glacier's mechanical response to the landfast ice condition in the LHB in detail, we calculated anomalies in the ice thickness and flow velocity of the Shirase Glacier for the three parts of the upstream, middle-stream, and downstream regions of the Shirase Glacier tongue (Figure 4). It shows that the response timing to changes in flow velocity and ice thickness due to the stability of landfast ice differed depending on the flow velocity and ice thickness among the glacier stream regions. The flow velocity in the upstream region showed a slight acceleration during periods of unstable landfast ice (Figure 4b), but the ice thickness showed no clear thinning associated with the stability of the landfast ice (Figure 4a). In the middle-stream region, the glacier ice generally thickened with large positive anomalies in 2021 and 2024, despite periods of stable or unstable landfast ice (Figure 4c). In the downstream region, the flow velocity anomalies shifted immediately to significant acceleration when the landfast ice broke away in 2017 and 2025 (Figure 4f). Subsequently, as the landfast ice stabilized in 2019, it changed to immediate deceleration. Hence, the flow velocity responds instantaneously to changes in the stability of landfast ice without a time lag. Furthermore, the ice thickness in the downstream region had a time lag before it changed to negative during periods of unstable landfast ice in 2017 and 2025 (Figure 4e).

To investigate the delayed response of ice thickness to accelerations in flow velocity, a lag correlation analysis was performed using the ice thickness and flow velocity anomalies in the downstream region. Given the limited number of data points over the decadal observation, we applied a bootstrap resampling method (10,000 iterations) to estimate the 95% confidence intervals (CI) for the Pearson correlation coefficients (r) at each lag step to evaluate the statistical robustness. The calculated statistics for the delayed response time of ice thickness to flow velocity fluctuations from zero to three years are as follows: for a 0-year lag ($N = 10$, $df = 8$), $r = -0.53$ ($p = 0.119$, 95% CI = $[-0.95, -0.11]$); for a 1-year lag ($N = 9$, $df = 7$), $r = -0.49$ ($p = 0.182$, 95% CI = $[-0.96, +0.62]$); for a 2-year lag ($N = 8$, $df = 6$), $r = -0.56$ ($p = 0.147$, 95% CI = $[-0.95, +0.94]$); for a 3-year lag ($N = 7$, $df = 5$), $r = +0.43$ ($p = 0.334$, 95% CI = $[-0.88, +0.92]$). Although the statistical significance is constrained by the limited sample size (N) and wide confidence intervals, the maximum negative correlation coefficient is observed at a 2-year lag before transitioning to a positive correlation at a 3-year lag. While we cannot definitively establish strict statistical significance, this temporal pattern suggests a potential dynamic time lag (approximately zero to two years) between the immediate flow acceleration caused by landfast ice breakaway and the subsequent physical mass loss (thinning) of the Shirase Glacier tongue. Furthermore, the sign reversal to a positive correlation at a 3-year lag ($r = +0.43$) is accompanied by a wide 95% confidence interval crossing zero (CI = $[-0.88, +0.92]$), indicating a lack of statistical significance. This reversal implies that the glacier system's delayed physical mass loss (thinning) potentially completes within approximately two years. Beyond this timeframe, the short-term periodic nature of

the landfast ice dynamics causes the correlation between velocity and thickness anomalies to completely break down.

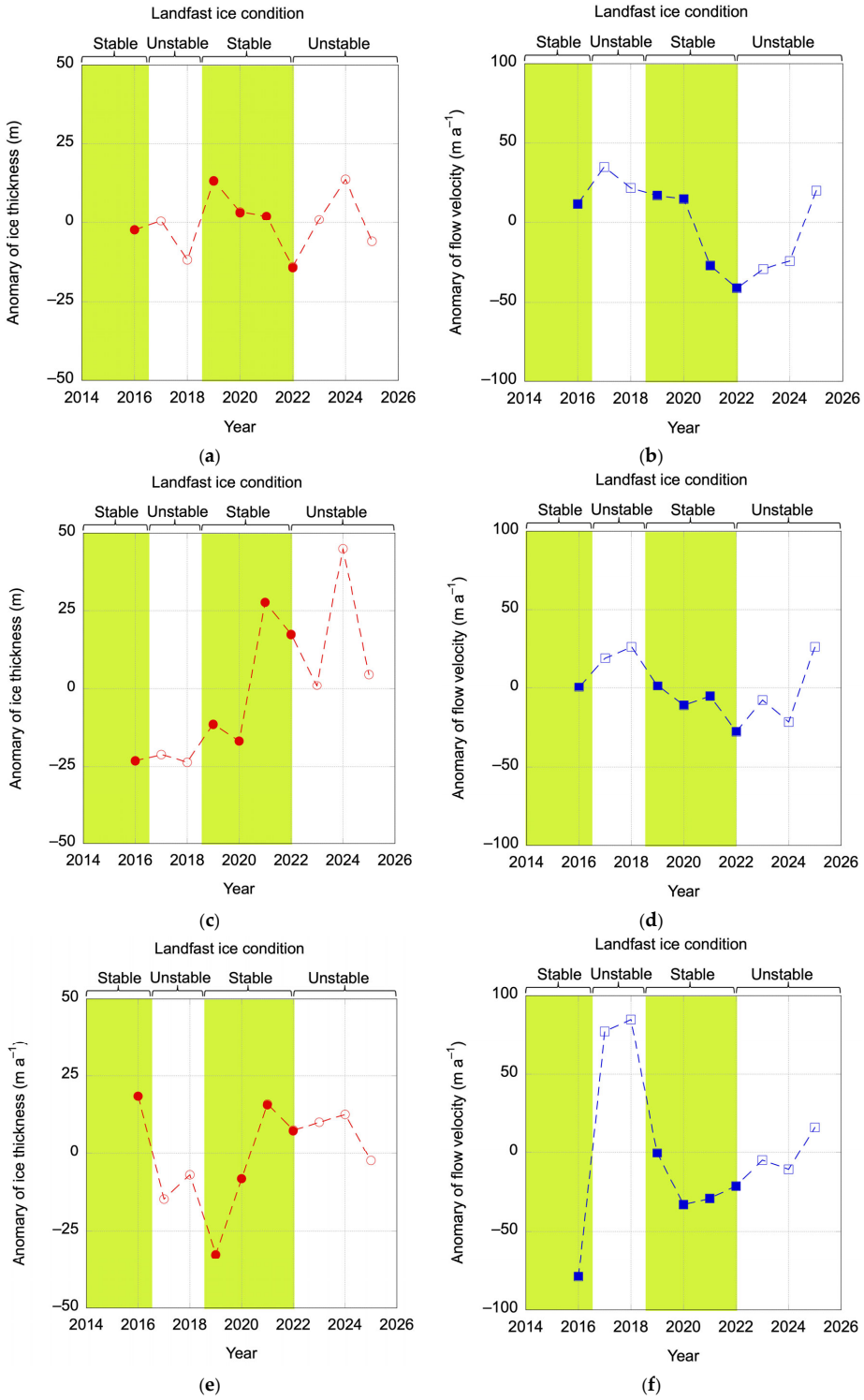


Figure 4. Relationship between ice thickness and flow velocity under stable and unstable landfast ice conditions. Solid and open plots are stable and unstable landfast ice conditions, respectively. Red markers indicate ice thickness, and blue markers indicate flow velocity. Anomalies were calculated by subtracting the decadal mean (2016–2025) from the annual mean values for each region. (**a**,**c**,**e**) are anomalies in ice thickness, while (**b**,**d**,**f**) are anomalies in flow velocity; (**a**,**b**) are anomalies in the upstream, (**c**,**d**) are anomalies in the middle-stream, and (**e**,**f**) are anomalies in the downstream regions. The yellow-green shaded areas indicate periods of stable landfast ice conditions in the LHB.

The different timescales of the mechanical response could be explained by the mechanisms of stress propagation and mass conservation in glaciers. The immediate response of the flow velocity to stable or unstable landfast ice was considered to result from drastic changes in the stress balance. The detailed physical mechanisms will be discussed in Section 4.

3.3. Relationship Between Ice Thickness and Flow Velocity Associated with Landfast Ice Stability

As a factor that causes interannual variability, this study examines how the stable or unstable condition of landfast ice in the LHB surrounding the Shirase Glacier terminus influenced the relationship between the ice thickness and flow velocity of the glacier. The relationship between the ice thickness and flow velocity of the glacier was therefore examined separately in three regions: upstream, middle-stream, and downstream. Figure 5 shows the relationship between ice thickness and flow velocity at (a) the upstream, (b) the middle stream, and (c) the downstream regions of the Shirase Glacier tongue. The ice thickness decreased as the flow velocity increased; hence, a negative correlation was observed in all regions, regardless of ice stability in the LHB. These results were similar to those in Figure 3. This can be explained by the law of mass conservation, which states that ice thickness and flow velocity are inversely proportional, provided that the ice flux of Shirase Glacier remains constant.

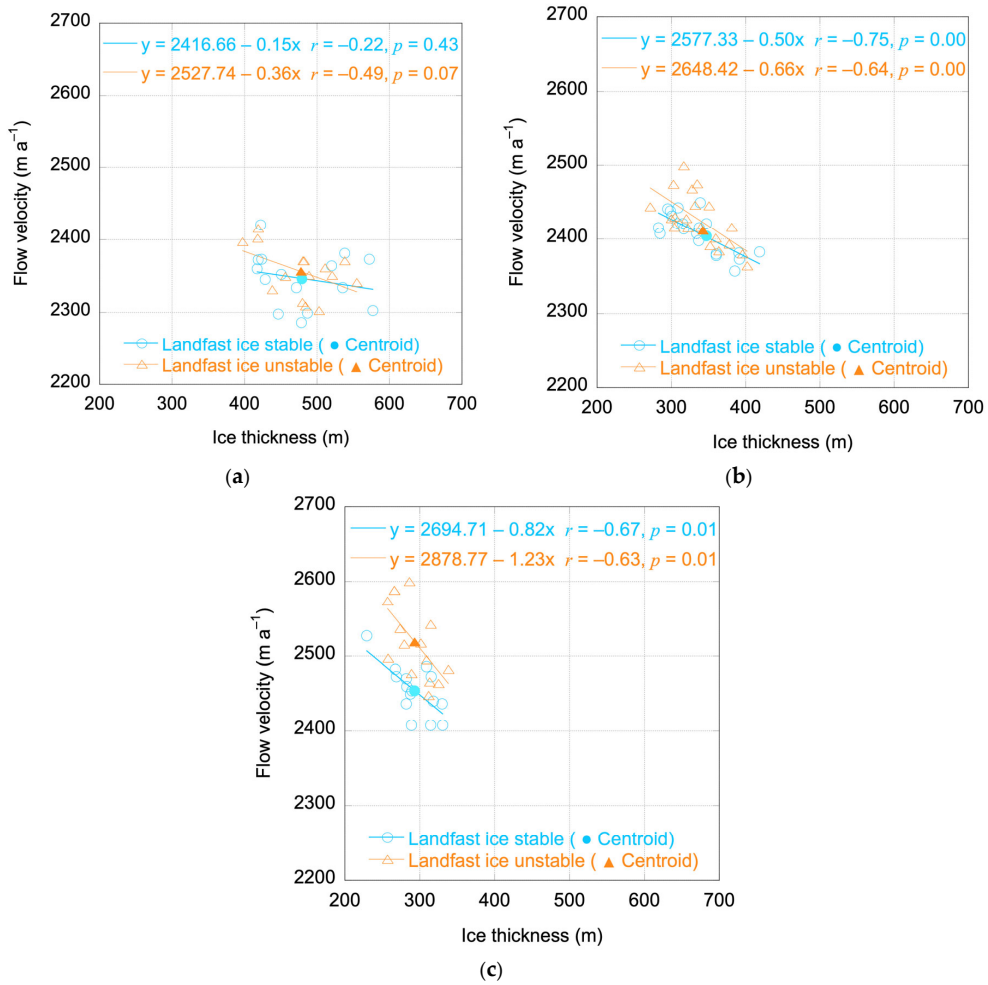


Figure 5. Relationship between ice thickness and flow velocity under stable and unstable landfast ice conditions in the LHB at (**a**) the upstream, (**b**) the middle-stream, and (**c**) the downstream regions of the Shirase Glacier tongue.

In the upstream (Figure 5a) and middle-stream (Figure 5b) regions, the relationships were almost the same regardless of the landfast ice stability, and the difference between their centroids (solid circles and triangles) would be negligible (<1%). Even if the landfast ice surrounding the glacier terminus were to break away in the LHB, the impact of the loss of its buttress effect may not immediately propagate to the upstream and middle-stream regions (up to 45 km DGL). Conversely, in the downstream region (Figure 5c), the difference in centroid between stable and unstable landfast ice was significant, and was found to be associated with the flow velocity acceleration by a mean of 3% (approximately 65 m a^{-1}) without any change in the ice thickness.

Therefore, in the upstream and middle-stream regions, no changes in ice thickness or flow velocity were observed regardless of the landfast ice stability. In the downstream region, in contrast, there was almost no change in the ice thickness, but a significant acceleration in the flow velocity was observed during the unstable landfast period. Thus, these results directly reveal the buttressing effect and its loss caused by changes in landfast ice conditions.

3.4. Basal Melt Rate Distribution

Next, the contributions of the second term (time derivative) and the third and fourth terms (spatial derivatives) on the right-hand side of Equation (7) were validated. Figure 6 shows the variations in the time derivative and spatial derivative terms of Equation (7). Based on the decadal mean estimates calculated from the satellite data, the temporal variation in ice thickness (the time derivative term) ranged from −1.3 to +2.9 m a^{-1} along the streamline. While the divergence of the ice flux (the spatial derivative term) ranged from −3.4 to −20.6 m a^{-1}, the spatial derivative term was found to dominate the right-hand side of Equation (7). A negative value for this spatial derivative term indicated that the outflow downstream was less than the inflow from upstream, resulting in a state where the ice was mechanically compressed and tends to thicken; and hence that means the ice flux convergence. In contrast, the magnitude of the temporal derivative term was only about one-tenth that of the spatial derivative term. This meant that the ice thickness of the glacier tongue remained in a relatively stable condition over the decade. However, the actual ice thickness did not show a significant increase despite this state of mechanical compression. This observation strongly suggests that the excess ice resulting from the compression was offset by basal melting, which appeared as the residual term in Equation (7).

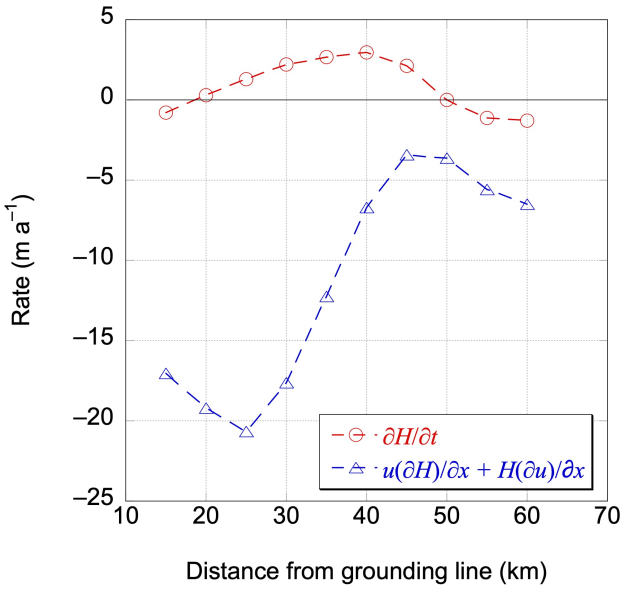


Figure 6. Variations in the time derivative and spatial derivative terms of Equation (7).

Figure 7 shows the decadal mean basal melt rate calculated using data acquired from 2016 to 2025, with the standard deviation represented by error bars. To calculate the basal melt rate, a Gaussian filter with a parameter $\sigma = 1.0$ was applied to both time and distance. Figure 7 shows a high melt rate of approximately 20 m a^{-1} between 15 and 25 km DGL. This suggests that the region from the GL to 25 km DGL experienced significant basal melt, which was strongly suggested to be associated with the intrusion of warm modified Circumpolar Deep Water (mCDW) underneath the Shirase Glacier tongue. The result was roughly consistent with the observation of basal melt rates between 7 and 16 m a^{-1} derived from ice radar observations at 16 km DGL [11], as well as with estimates of 6–13 m a^{-1} from a basal melt model for the Shirase Glacier [12].

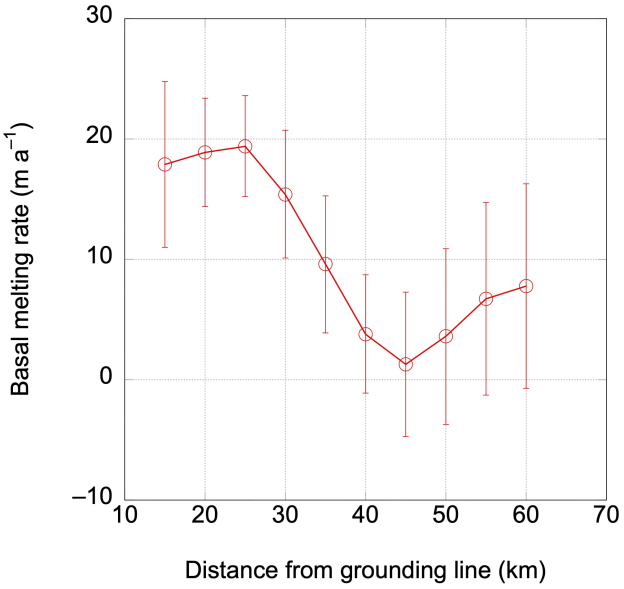


Figure 7. Mean and SD basal melting rate of Shirase Glacier from 2016 to 2025.

4. Discussion

4.1. Oceanographic Interpretation of Basal Melting

The basal melting of the Shirase Glacier tongue was observed up to 35 km DGL, but the melt rate decreased to a few m a^{-1} beyond 35 km DGL, extending to 45 km DGL. This is because the thermal forcing of the seawater decreased discontinuously as the glacier tongue contacted the cold upper layer of winter water near the freezing-point temperature of seawater. Further downstream, greater basal melting was observed again at 50–60 km DGL. Since that region is close to the calving front, the warmed summer surface water is expected to intrude into the ice front of the glacier and then potentially promote a higher basal melt (e.g., [35]). Therefore, the results of the basal melt rate calculation were found to be consistent with the processes of ocean circulation under the tongue of the Shirase Glacier.

While a previous regional ocean model by [12] supports the broad mechanism of mCDW intrusion into LHB, their simulated spatial pattern of basal melting showed higher rates near the ice front and lower rates near the grounding line. This discrepancy likely arises from the spatial resolution constraints (<2.5 km) of their model, which resulted in an unrealistic representation of the ice draft that deepens again near the glacier terminus (as shown in their Figure 1). This overestimated deep draft at the seaward edge artificially increases the contact area with the inflowing warm deep water, leading to overestimated melting at the front. Our observational results, directly derived from high-resolution satellite data, overcome these geometric modeling limitations and provide a more realistic spatial distribution of basal melting along the Shirase Glacier tongue.

4.2. Mechanical Response of Shirase Glacier to Landfast Ice Dynamics

A glacier experiences a loss of back pressure when the landfast ice collapses and flows away. Consequently, the longitudinal tensile stress within the ice tongue increases instantaneously [3]. Since stress changes propagate through the ice body extremely rapidly, the flow velocity accelerates immediately without any time lag, which is highly correlated with the loss of landfast ice supporting the glacier terminus [5,6]. In fact, the flow velocity anomalies in the upstream region (15–25 km DGL) also showed a slight acceleration during the landfast ice instability in the LHB in 2017 and 2025. This suggests that stress changes also propagate rapidly through the upstream region of Shirase Glacier.

The delayed response of ice thickness of the glacier to the stability or instability of the landfast ice in the LHB is plausibly explained by the cumulative process of mass changes caused by the mechanical deformation (elongation) associated with the acceleration of the flow velocity of Shirase Glacier. According to the continuity Equation (7), the ice thickness changes in glaciers are determined by the divergence of ice flux. Hence, this divergence is determined by the balance between the elongated ice due to flow and its mass. Even if the ice flow in the downstream region of the glacier is accelerated immediately due to landfast ice instability, a temporal integration process is required by accumulating ice mass discharge before the ice is actually thinned physically. The time lag of one to two years observed in this study was probably the result of the time required for the deformation. In the upstream region, slight acceleration due to stress propagation was observed; however, the outflow of ice mass was not sufficient to decrease the ice thickness. Furthermore, the ice thickness anomaly in the middle-stream region (30–45 km DGL) was less associated with the dynamics of the landfast ice, but independent fluctuations were observed. This is probably because the anomaly was dominated by a different oceanic process, such as basal melting discussed above.

Therefore, the Shirase Glacier tongue is found to respond (accelerate) sensitively and directly to changes in the landfast ice dynamics in the LHB. Consequently, this study quantitatively demonstrated that there was a glacial dynamic lag before this response manifested as actual mass changes (thinning), and that the effects propagate while attenuating both spatially and dynamically.

4.3. Limitations and Uncertainties

While this study elucidates the dynamic relationship between landfast ice and glacier flow, several limitations must be acknowledged. First, the causal interpretation between landfast ice breakaway and flow acceleration is strongly suggested by temporal correlation, but direct in situ mooring observations beneath the ice tongue during the specific analysis period are lacking. Furthermore, although the spatial distribution of the estimated basal melt aligns with the known vertical thermal structure of modified Circumpolar Deep Water (mCDW) [11], contemporaneous direct oceanographic monitoring is required to fully validate this relationship.

Second, estimating basal melt rates using the 1D Eulerian flux divergence method along the central streamline assumes a constant flow width and negligible transverse strain rates. As the outlet glacier flows downstream and loses lateral confinement from the bedrock walls, the ice tongue tends to spread laterally. This lateral expansion induces transverse strain rates that allow ice mass to flow outward from the central streamline. Neglecting this lateral divergence can lead to an overestimation of the longitudinal ice flux convergence, which in turn could result in an overestimation of the calculated basal melt rates derived as the residual. However, as the two-dimensional velocity vector fields from our recent study [13] demonstrate, the glacier is laterally constrained by the bedrock topography, making the transverse velocity component at least an order of magnitude smaller than the

highly directional longitudinal flow. Thus, the quantitative impact of this lateral spreading is expected to be relatively limited. Therefore, while our 1D approximation captures the primary longitudinal dynamics, future studies incorporating 2D or 3D ice flow field data are required to quantify the exact contribution of the transverse strain rates.

5. Conclusions

This study analyzed the spatiotemporal variations in flow velocity and ice thickness of the Shirase Glacier ice tongue using continuous satellite observation data from the ALOS-2/PALSAR-2 and the CryoSat-2/SIRAL. Moreover, we calculated the basal melt rate by applying the Eulerian flux divergence method based on the law of mass conservation. This calculation utilized the satellite-derived flow velocity and ice thickness, alongside the surface mass balance (SMB) from the RACMO model.

The decadal satellite observations from 2016 to 2025 revealed spatial fluctuations in which the ice thickness decreased as its flow velocity increased toward the downstream region. This relationship between ice thickness and flow velocity can be qualitatively explained by the continuity equation. Furthermore, it was shown that the contribution of ice thickness decreases associated with increasing flow velocity was higher in the upstream region of the glacier tongue than in the downstream region. From 2017 to 2018 and from 2023 to 2025, when landfast ice at the glacier terminus broke away under unstable landfast ice conditions, there was no significant change in ice thickness, but flow velocity accelerated by 3%, especially in the downstream region. Therefore, the Shirase Glacier tongue is found to respond (accelerate) sensitively and directly to changes in the landfast ice dynamics in the LHB. Consequently, this study suggests a potential glacial dynamic lag before this response manifested as actual mass changes (thinning), and that the effects propagate while attenuating both spatially and dynamically.

The basal melt rate of the Shirase Glacier, taking into account the temporal variations in ice thickness, was determined using the Eulerian flux divergence method. Around the region of 15–25 km DGL, a high melt rate of approximately 20 m a^{-1} is obtained, which is thought to be associated with the warm inflow of mCDW. Subsequently, the melt rate decreased to a few m a^{-1} from 35 km DGL toward 45 km DGL. The melt rate increased towards the glacier terminus at 50–60 km DGL, potentially driven by the warmed offshore seawater intruding into the ice front of the glacier.

This study quantitatively demonstrated that spatiotemporal variations in the Shirase Glacier's flow are strongly influenced by both landfast ice fluctuations and subglacial ocean circulation processes. These findings provide an important contribution to our understanding of the complex interactions among glaciers, landfast ice, and the ocean in East Antarctica.

Overall, the primary contributions of this study to the understanding of Antarctic ice shelf dynamics are twofold. First, we provided a novel quantitative assessment of the delayed mechanical response of the Shirase Glacier, suggesting a potential dynamic time lag of approximately zero to two years between the immediate flow acceleration triggered by landfast ice breakaway and subsequent ice thinning. Second, we clarified the spatial differentiation of basal melt drivers along the floating ice tongue; our results suggest that the deep grounding zone is primarily influenced by the intrusion of modified Circumpolar Deep Water (mCDW), whereas the region near the calving front is more likely affected by warmed summer surface water. These findings offer critical insights into the complex ice–ocean interactions and will contribute to improving future mass balance projections of Antarctic fast-flowing outlet glaciers.

https://doi.org/10.3390/rs18213849

Author Contributions: Conceptualization, K.N.; methodology, K.N. and Y.S.; software, K.N. and Y.S.; validation, K.N., Y.S., T.Y. and S.A.; formal analysis, K.N.; investigation, K.N.; resources, K.N.; data curation, K.N.; writing—original draft preparation, K.N.; writing—review and editing, K.N., Y.S., T.Y. and S.A.; visualization, K.N.; supervision, S.A. and K.N.; project administration, K.N.; funding acquisition, K.N. All authors have read and agreed to the published version of the manuscript.

Funding: This work was funded in part by the Grants-in-Aid for Scientific Research of the MEXT/JSPS of the Japanese Government (26K15146), and in part by the Joint Research Program of the Institute of Low Temperature Science, Hokkaido University (26G042).

Data Availability Statement: The ALOS-2/PALSAR-2 data were obtained from JAXA through the 3rd and 4th Earth observation research announcements at https://earth.jaxa.jp/en/research/cooperation/ra3/index.html (accessed on 20 September 2026) and https://earth.jaxa.jp/en/research/cooperation/ra4/index.html, respectively (accessed on 20 September 2026). The CryoSat-2/SIRAL data are available at https://cs2eo.org/ (accessed on 20 September 2026). The AMSR2 data are available at JAXA's AMSR Research Product Distribution Service at https://www.eorc.jaxa.jp/AMSR/research/index_en.html (accessed on 20 September 2026). The MODIS images are available at the Arctic and Antarctic Data Archive System of the National Institute of Polar Research at https://ads.nipr.ac.jp/ (accessed on 27 October 2026).

Acknowledgments: The authors express sincere thanks to anonymous reviewers for critically reading and improving the manuscript. This work was supported in part by the Grants-in-Aid for Scientific Research of the MEXT/JSPS of the Japanese Government (26K15146), and in part by the Joint Research Program of the Institute of Low Temperature Science, Hokkaido University (26G042).

Conflicts of Interest: The authors declare no conflicts of interest.

Appendix A

Tables A1 and A2 list observation pairs of the PALSAR-2 in this study whose path numbers are 193 and 195, respectively.

Table A1. Path 193.

Primary	Secondary
14 April 2016	28 April 2016
13 October 2016	27 October 2016
30 March 2017	13 April 2017
14 September 2017	28 September 2017
26 October 2017	9 November 2017
29 March 2018	12 April 2018
27 September 2018	11 October 2018

Table A2. Path 195.

Primary	Secondary	Primary	Secondary
1 July 2018	12 August 2018	16 May 2021	30 May 2021
12 August 2018	21 October 2018	27 June 2021	11 July 2021
21 October 2018	4 November 2018	11 July 2021	25 July 2021
4 November 2018	30 December 2018	25 July 2021	8 August 2021
13 January 2019	27 January 2019	8 August 2021	22 August 2021
27 January 2019	24 February 2019	22 August 2021	5 September 2021
24 February 2019	10 March 2019	17 October 2021	31 October 2021
10 March 2019	24 March 2019	31 October 2021	14 November 2021
24 March 2019	7 April 2019	9 January 2022	23 January 2022
7 April 2019	21 April 2019	6 May 2022	20 May 2022

Table A2. *Cont*.

Primary	Secondary	Primary	Secondary
21 April 2019	5 May 2019	20 May 2022	3 April 2022
5 May 2019	19 May 2019	26 June 2022	10 July 2022
19 May 2019	2 June 2019	10 July 2022	24 July 2022
2 June 2019	16 June 2019	24 July 2022	7 August 2022
16 June 2019	30 June 2019	7 August 2022	21 August 2022
30 June 2019	14 July 2019	16 October 2022	30 October 2022
14 July 2019	28 July 2019	30 October 2022	13 November 2022
28 July 2019	11 August 2019	8 January 2023	22 January 2023
11 August 2019	25 August 2019	5 May 2023	19 May 2023
25 August 2019	8 September 2019	19 May 2023	2 April 2023
20 October 2019	3 November 2019	2 April 2023	16 April 2023
3 November 2019	17 November 2019	16 April 2023	30 April 2023
17 November 2019	1 December 2019	25 June 2023	9 July 2023
1 December 2019	29 December 2019	6 August 2023	20 August 2023
12 January 2020	26 January 2020	20 August 2023	3 September 2023
26 January 2020	23 February 2020	15 October 2023	29 October 2023
23 February 2020	22 March 2020	29 October 2023	12 November 2023
22 March 2020	5 April 2020	7 January 2024	21 January 2024
5 April 2020	19 April 2020	3 May 2024	17 May 2024
19 April 2020	3 May 2020	17 May 2024	31 May 2024
3 May 2020	14 June 2020	31 May 2024	14 April 2024
14 June 2020	28 June 2020	14 April 2024	28 April 2024
28 June 2020	12 July 2020	23 June 2024	7 July 2024
12 July 2020	26 July 2020	7 July 2024	21 July 2024
26 July 2020	23 August 2020	5 January 2025	19 January 2025
23 August 2020	1 November 2020	2 May 2025	16 May 2025
1 November 2020	15 November 2020	16 May 2025	30 May 2025
15 November 2020	29 November 2020	30 May 2025	13 April 2025
10 January 2021	12 January 2021	13 April 2025	27 April 2025
2 May 2021	16 May 2021	6 September 2025	20 September 2025

Appendix B

Table A3 summarizes the details of the SIRAL data acquisition dates in this study.

Table A3. After screening SIRAL data acquisition dates.

Date/Orbit	Date/Orbit	Date/Orbit	Date/Orbit
21 January 2016/Descending	20 May 2018/Descending	28 March 2021/Ascending	30 December 2023/Ascending
26 January 2016/Ascending	20 July 2018/Ascending	12 May 2021/Descending	13 February 2024/Descending
19 February 2016/Descending	13 August 2018/Descending	6 June 2021/Descending	9 March 2024/Descending
20 April 2016/Ascending	13 October 2018/Ascending	1 July 2021/Descending	3 April 2024/Descending
14 May 2016/Descending	11 November 2018/Ascending	4 July 2021/Ascending	6 April 2024/Ascending
11 June 2016/Descending	5 December 2018/Descending	12 September 2021/Descending	1 May 2024/Ascending
14 July 2016/Ascending	6 January 2019/Ascending	6 October 2021/Descending	26 May 2024/Ascending
6 August 2016/Descending	27 February 2019/Descending	4 November 2021/Ascending	9 July 2024/Descending
12 August 2016/Ascending	30 April 2019/Ascending	12 January 2022/Descending	3 August 2024/Descending
4 September 2016/Descending	23 May 2019/Descending	6 February 2022/Descending	7 August 2024/Ascending
7 October 2016/Ascending	24 July 2019/Ascending	7 March 2022/Ascending	1 September 2024/Ascending
30 October 2016/Descending	16 August 2019/Descending	15 May 2022/Descending	26 September 2024/Ascending
5 November 2016/Ascending	14 September 2019/Descending	9 June 2022/Descending	9 November 2024/Descending
28 November 2016/Descending	16 October 2019/Ascending	4 July 2022/Descending	4 December 2024/Descending
23 January 2017/Descending	9 November 2019/Descending	29 July 2022/Descending	8 December 2024/Ascending
29 January 2017/Ascending	14 November 2019/Ascending	26 August 2022/Ascending	2 January 2025/Ascending
21 February 2017/Descending	2 February 2020/Descending	20 September 2022/Ascending	21 January 2025/Descending
23 April 2017/Ascending	7 February 2020/Ascending	4 November 2022/Descending	15 February 2025/Descending
17 May 2017/Descending	2 March 2020/Descending	29 November 2022/Descending	12 March 2025/Descending

Table A3. *Cont.*

Date/Orbit	Date/Orbit	Date/Orbit	Date/Orbit
17 July 2017/Ascending	2 May 2020/Ascending	6 March 2023/Descending	6 April 2025/Descending
10 August 2017/Descending	25 May 2020/Descending	31 March 2023/Descending	9 April 2025/Ascending
8 September 2017/Descending	26 July 2020/Ascending	29 April 2023/Ascending	4 May 2025/Ascending
10 October 2017/Ascending	3 October 2020/Descending	24 May 2023/Ascending	16 July 2025/Ascending
2 November 2017/Descending	1 November 2020/Ascending	7 July 2023/Descending	23 September 2025/Descending
26 January 2018/Descending	26 November 2020/Ascending	1 August 2023/Descending	27 September 2025/Ascending
1 February 2018/Ascending	9 January 2021/Descending	30 August 2023/Ascending	22 October 2025/Ascending
24 February 2018/Descending	3 February 2021/Descending	24 September 2023/Ascending	16 November 2025/Ascending
27 April 2018/Ascending	3 March 2021/Ascending	7 November 2023/Descending	30 December 2025/Descending

References

1. Pritchard, H.D.; Ligtenberg, S.R.M.; Fricker, H.A.; Vaughan, D.G.; van den Broeke, M.R.; Padman, L. Antarctic ice-sheet loss driven by basal melting of ice shelves. *Nature* **2012**, *484*, 502–505. [CrossRef] [PubMed]
2. Rignot, E.; Jacobs, S.; Mouginot, J.; Scheuchl, B. Ice-shelf melting around Antarctica. *Science* **2013**, *341*, 266–270. [CrossRef] [PubMed]
3. Dupont, T.K.; Alley, R.B. Assessment of the importance of ice-shelf buttressing to ice-sheet stability. *Geophys. Res. Lett.* **2005**, *32*, L22503. [CrossRef]
4. Gudmundsson, G.H. Ice-shelf buttressing and the stability of marine ice sheets. *The Cryosphere* **2013**, *7*, 647–655. [CrossRef]
5. Rignot, E.; Casassa, G.; Gogineni, P.; Krabill, W.; Rivera, A.; Thomas, R. Accelerated ice discharge from the Antarctic Peninsula following the collapse of Larsen B ice shelf. *Geophys. Res. Lett.* **2004**, *31*, L18401. [CrossRef]
6. Scambos, T.A.; Bohlander, J.A.; Shuman, C.A.; Skvarca, P. Glacier acceleration and thinning after ice shelf collapse in the Larsen B embayment, Antarctica. *Geophys. Res. Lett.* **2004**, *31*, L18402. [CrossRef]
7. Fürst, J.J.; Durand, G.; Gillet-Chaulet, F.; Tavard, L.; Rank, M.; Braun, M.; Gagliardini, O. The safety band of Antarctic ice shelves. *Nat. Clim. Change* **2016**, *6*, 479–482. [CrossRef]
8. Massom, R.A.; Scambos, T.A.; Bennetts, L.G.; Reid, P.; Squire, V.A.; Stammerjohn, S.E. Antarctic ice shelf disintegration triggered by sea ice loss and ocean swell. *Nature* **2018**, *558*, 383–389. [CrossRef] [PubMed]
9. Miles, B.W.J.; Stokes, C.R.; Jamieson, S.S.R. Pan–ice-sheet glacier terminus change in East Antarctica reveals sensitivity of Wilkes Land to sea-ice changes. *Sci. Adv.* **2016**, *2*, e1501350. [CrossRef] [PubMed]
10. Nakamura, K.; Yamanokuchi, T.; Doi, K.; Shibuya, K. Net mass balance calculations for the Shirase drainage basin, East Antarctica. *Polar Sci.* **2016**, *10*, 111–122. [CrossRef]
11. Hirano, D.; Tamura, T.; Kusahara, K.; Ohshima, K.I.; Nicholls, K.W.; Ushio, S.; Simizu, D.; Ono, K.; Fujii, M.; Nogi, Y.; et al. Strong ice-ocean interaction beneath Shirase Glacier tongue in East Antarctica. *Nat. Commun.* **2020**, *11*, 4221. [CrossRef] [PubMed]
12. Kusahara, K.; Hirano, D.; Fujii, M.; Fraser, A.D.; Tamura, T. Modeling intensive ocean-cryosphere interactions in Lützow-Holm Bay, East Antarctica. *Cryosphere* **2021**, *15*, 1697–1717. [CrossRef]
13. Nakamura, K.; Aoki, S.; Yamanokuchi, T.; Tamura, T.; Doi, K. Validation for ice flow velocity variations of Shirase Glacier derived from PALSAR-2 offset tracking. *IEEE J. Sel. Top. Appl. Earth Obs. Remote Sens.* **2022**, *15*, 3269–3281. [CrossRef]
14. Miles, B.W.J.; Stokes, C.R.; Jenkins, A.; Jordan, J.R.; Jamieson, S.S.R.; Gudmundsson, G.H. Slowdown of Shirase Glacier, East Antarctica, caused by strengthening alongshore winds. *The Cryosphere* **2023**, *17*, 445–456. [CrossRef]
15. Gerrish, L.; Ireland, L.; Fretwell, P.; Cooper, P.; Skachkova, A. *High Resolution Vector Polylines of the Antarctic Coastline (Version 7.11) [Data Set]*; NERC EDS UK Polar Data Centre: Cambridge, UK, 2021. [CrossRef]
16. Arctic and Antarctic Data archive System. Available online: https://ads.nipr.ac.jp/ (accessed on 27 October 2026).
17. Jezek, K.C.; Curlander, J.C.; Carsey, F.; Wales, C.; Barry, R.G. *RAMP AMM-1 SAR Image Mosaic of Antarctica, Version 2*; NASA National Snow and Ice Data Center Distributed Active Archive Center: Boulder, CO, USA, 2013. [CrossRef]
18. Rignot, E.; Mouginot, J.; Scheuchl, B. Ice Flow of the Antarctic Ice Sheet. *Science* **2011**, *333*, 1427–1430. [CrossRef] [PubMed]
19. Pavlis, N.K.; Holmes, S.A.; Kenyon, S.C.; Factor, J.K. The development and evaluation of the Earth Gravitational Model 2008 (EGM2008). *J. Geophys. Res. Solid Earth* **2012**, *117*, B04406. [CrossRef]
20. Vaughan, D.G. Tidal flexure at ice shelf margins. *J. Geophys. Res. Solid Earth* **1995**, *100*, 6213–6224. [CrossRef]
21. Satake, Y.; Nakamura, K. Temporal variations in ice thickness of the Shirase Glacier derived from CryoSat-2/SIRAL data. *Remote Sens.* **2023**, *15*, 1205. [CrossRef]
22. Kawamura, T.; Ohshima, K.I.; Takizawa, T.; Ushio, S. Physical, structural, and isotopic characteristics and growth processes of fast sea ice in Lützow-Holm Bay, Antarctica. *J. Geophys. Res. Oceans* **1997**, *102*, 3345–3355. [CrossRef]
23. AMSR Research Product Distribution Service. Available online: https://www.eorc.jaxa.jp/AMSR/research/index_en.html (accessed on 20 September 2026).

24. Kwok, R. Satellite remote sensing of sea-ice thickness and kinematics: A review. *J. Glaciol*. **2010**, *56*, 1129–1140. [CrossRef]
25. Kwok, R. Simulated effects of a snow layer on retrieval of CryoSat-2 sea ice freeboard. *Geophys. Res. Lett*. **2014**, *41*, 5014–5020. [CrossRef]
26. Kelly, R.; Li, Q.; Saberi, N. The AMSR2 satellite-based microwave snow algorithm (SMSA): A new algorithm for estimating global snow accumulation. In Proceedings of the 2019 IEEE International Geoscience and Remote Sensing Symposium (IGARSS), Yokohama, Japan, 28 July–2 August 2019; pp. 4335–4338. [CrossRef]
27. Ricker, R.; Hendricks, S.; Helm, V.; Skourup, H.; Davidson, M. Sensitivity of CryoSat-2 Arctic sea-ice freeboard and thickness on radar-waveform interpretation. *Cryosphere* **2014**, *8*, 1607–1622. [CrossRef]
28. Cuffey, K.M.; Paterson, W.S.B. *The Physics of Glaciers*, 4th ed.; Butterworth-Heinemann: Oxford, UK, 2010.
29. Adusumilli, S.; Fricker, H.A.; Medley, B.; Padman, L.; Siegfried, M.R. Interannual variations in meltwater input to the Southern Ocean from Antarctic ice shelves. *Nat. Geosci*. **2020**, *13*, 616–620. [CrossRef] [PubMed]
30. van Dalum, C.; van de Berg, W.J.; van den Broeke, M.; Hofsteenge, M. The surface mass balance and near-surface climate of the Antarctic ice sheet in RACMO2.4p1. *Cryosphere* **2025**, *19*, 4061–4090. [CrossRef]
31. Nakamura, K.; Aoki, S.; Yamanokuchi, T.; Tamura, T. Interactive movements of outlet glacier tongue and landfast sea ice in Lützow-Holm Bay, East Antarctica, detected by ALOS-2/PALSAR-2 imagery. *Sci. Remote Sens*. **2022**, *5*, 100064. [CrossRef]
32. Nakamura, K.; Yamanokuchi, T.; Aoki, S.; Doi, K.; Shibuya, K. Temporal variations in the flow velocity for Shirase Glacier in Antarctica over a 20-year period. *Seppyo* **2017**, *79*, 3–15. [CrossRef] [PubMed]
33. Nakamura, K.; Doi, K.; Shibuya, K. Fluctuations in the flow velocity of the Antarctic Shirase Glacier over an 11-year period. *Polar Sci*. **2010**, *4*, 443–455. [CrossRef]
34. Takaku, J.; Tadono, T.; Tsutsui, K.; Ichikawa, M. Validation of 'AW3D' Global DSM generated from ALOS PRISM. *ISPRS Ann. Photogramm. Remote Sens. Spat. Inf. Sci*. **2016**, *III-4*, 25–31. [CrossRef]
35. Aoki, S.; Takahashi, T.; Yamazaki, K.; Hirano, D.; Ono, K.; Kusahara, K.; Tamura, T.; Williams, G.D. Warm surface waters increase Antarctic ice shelf melt and delay bottom water formation. *Commun. Earth Environ*. **2022**, *3*, 142. [CrossRef]

Disclaimer/Publisher's Note: The statements, opinions and data contained in all publications are solely those of the individual author(s) and contributor(s) and not of MDPI and/or the editor(s). MDPI and/or the editor(s) disclaim responsibility for any injury to people or property resulting from any ideas, methods, instructions or products referred to in the content.